

“ORPHAN” γ -RAY FLARES AND STATIONARY SHEATHS OF BLAZAR JETS

NICHOLAS R. MACDONALD¹, SVETLANA G. JORSTAD^{1,2}, AND ALAN P. MARSCHER¹

¹Institute for Astrophysical Research, Boston University, 725 Commonwealth Avenue, Boston, MA 02215

²Astronomical Institute, St. Petersburg State University, Universitetskij Pr. 28, Petrodvorets, 198504 St. Petersburg, Russia

Draft version December 1, 2016

ABSTRACT

Blazars exhibit flares across the entire electromagnetic spectrum. Many γ -ray flares are highly correlated with flares detected at longer wavelengths; however, a small subset appears to occur in isolation, with little or no correlated variability at longer wavelengths. These “orphan” γ -ray flares challenge current models of blazar variability, most of which are unable to reproduce this type of behavior. MacDonald et al. have developed the *Ring of Fire* model to explain the origin of orphan γ -ray flares from within blazar jets. In this model, electrons contained within a blob of plasma moving relativistically along the spine of the jet inverse-Compton scatter synchrotron photons emanating off of a ring of shocked sheath plasma that enshrouds the jet spine. As the blob propagates through the ring, the scattering of the ring photons by the blob electrons creates an orphan γ -ray flare. This model was successfully applied to modeling a prominent orphan γ -ray flare observed in the blazar PKS 1510–089. To further support the plausibility of this model, MacDonald et al. presented a stacked radio map of PKS 1510–089 containing the polarimetric signature of a sheath of plasma surrounding the spine of the jet. In this paper, we extend our modeling and stacking techniques to a larger sample of blazars: 3C 273, 4C 71.01, 3C 279, 1055+018, CTA 102, and 3C 345, the majority of which have exhibited orphan γ -ray flares. We find that the model can successfully reproduce these flares, while our stacked maps reveal the existence of jet sheaths within these blazars. Our model points to the existence of a region of γ -ray production in blazars located outside of the most commonly considered regions in blazar jets, namely, the broad emission-line region (BLR), dusty molecular torus, and millimeter-wave “core”.

Subject headings: blazars: non-thermal radiative transfer - relativistic processes

1. INTRODUCTION

Many supermassive black hole systems at the centers of galaxies produce relativistic jets that propagate from sub-parsec to kilo-parsec scales. These radio jets emit synchrotron radiation due to the presence of electrons gyrating about magnetic field lines within the jet. A sub-set of these radio jets are closely aligned to our line-of-sight. These aligned jets are referred to as “blazars”. At 43 GHz, a VLBI image of a blazar typically exhibits a bright stationary feature known as the “radio core”. It has been postulated that the radio core of a blazar imaged at millimeter wavelengths is associated with a standing recollimation shock (resulting from pressure imbalance between the jet and its surroundings) several parsecs downstream of the central super-massive black hole of the system (see Marscher et al. 2008; Cawthorne, Jorstad, & Marscher 2013; Dodson et al. 2016 and references therein). Over the course of time, “blobs” of plasma are ejected from the radio core and propagate down the jet at relativistic speeds, which can appear superluminal in the observer’s frame. These blobs could be either internal shock waves propagating through the jet (see, e.g., Joshi & Böttcher 2011) or plasmoids with higher density and/or magnetic field than the ambient flow (the view adopted in this paper).

Blazars emit light across the entire electromagnetic spectrum, from low-energy radio waves to high-energy γ -rays. With the launch of the Fermi Large Area Telescope (LAT), it has become apparent (as hinted by EGRET) that the γ -ray sky outside the plane of the Milky Way is

dominated by blazar emission. Blazars are highly variable with timescales of γ -ray variability ranging from months, to days, and even minutes (e.g., Aharonian et al. 2007). Prominent γ -ray flares tend to be correlated with flares observed at longer wavelengths (e.g., in the optical and the radio; Marscher et al. 2012). There is, however, a small sub-set of “orphan” γ -ray flares that seem to occur in relative isolation, with little or no corresponding variability detected at longer wavelengths. Standard shock models of blazar emission have difficulty reproducing orphan γ -ray flares.

MacDonald et al. (2015) have developed the *Ring of Fire* model to explain the origin of orphan γ -ray flares from within a blazar jet. In this model, a segment (or ring) of a shocked non-relativistic sheath of plasma creates a localized source of synchrotron photons within the jet. These photons are inverse-Compton scattered up to high energies by electrons contained within a blob of plasma propagating relativistically down the spine of the jet (see “upstream” portion of Figure 1). The inverse-Compton scattering of the ring photons by the blob electrons creates an orphan γ -ray flare as the blob passes through the ring of shocked sheath. This model is able to successfully reproduce a prominent orphan γ -ray flare observed within the blazar PKS 1510–089 (see Marscher et al. 2010).

In order to verify the existence of a sheath of plasma surrounding the spine of the jet in PKS 1510–089, MacDonald et al. (2015) implemented a method of radio map stacking (in Stokes I, Q, and U) in order to detect the faint polarimetric signature of the jet sheath, which is

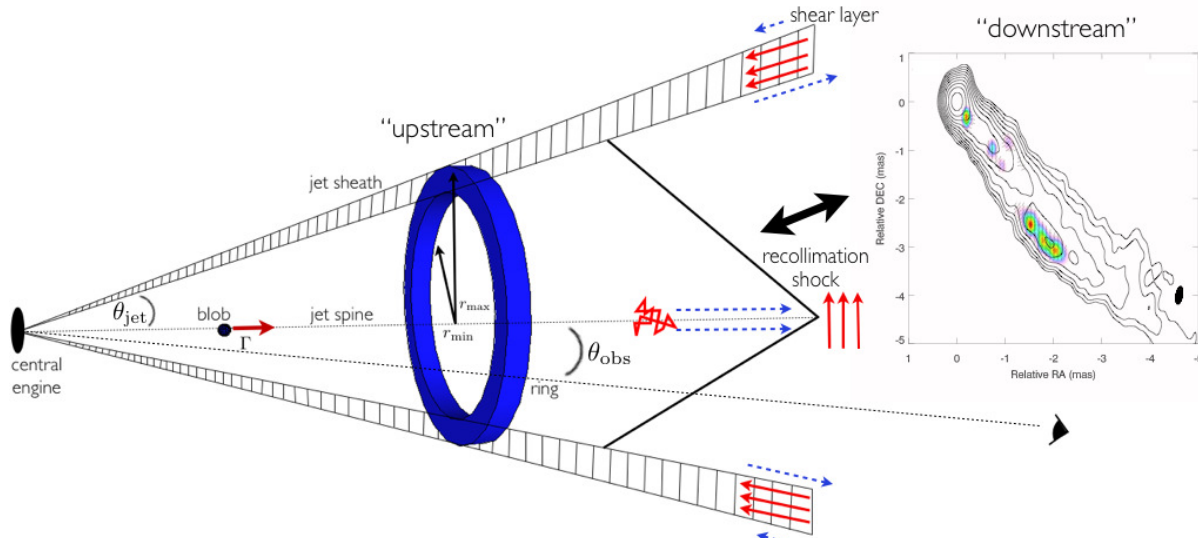


FIG. 1.— A schematic of the relative locations along the jet of both the ring of shocked sheath plasma in our model and the location of the radio core/sheath detected farther “downstream” in the stacked radio images of 3C 273 (see Figures 2 and 3). This sketch is projected onto the plane of the sky. We posit that the ring is located ~ 4 pc from the central engine, while the radio cores in our stacked maps are located farther downstream from the central engine (at a scale of $\gtrsim 10$ pc). We propose that the radio core in 3C 273 is associated with a recollimation shock that compresses initially tangled magnetic field along the spine of the jet and orders that field perpendicular to the jet axis (the red vectors just to the right of the recollimation shock). The jet has an opening angle $\lesssim 2^\circ$ and the recollimation shock subtends an angle to the jet axis $\lesssim 10^\circ$. In contrast to the spine, velocity shear between the sheath and the ambient medium (blue vectors denote relative speed) aligns the magnetic field lines on the outer edges of the jet to be roughly parallel to the jet axis, resulting in the spine-sheath polarization signature we detect in our stacked map of 3C 273 (shown in the “downstream” portion of this Figure and in Figure 3).

intrinsically far less luminous than the highly Doppler beamed spine. As discussed in Wardle et al. (1994), if the jet sheath represents a “shear layer” between the relativistic jet and the environment into which the jet propagates, one would expect the shear between the jet and the surrounding environment to “stretch out” the initially helical or tangled magnetic field of the jet and align it parallel to the jet axis. The observational signature of a shear layer would then be an increase in the observed fractional linear polarization towards the edges of the jet, with the orientation of that polarization being indicative of magnetic field that is aligned parallel to the jet axis. The orientation of polarized radio emission is delineated by the electric vector position angle (EVPA). The EVPA angle (χ) within a given pixel is computed based on the values of Stokes Q and U within that pixel: $\chi = \frac{1}{2} \arctan(U/Q)$. Barring the effects of relativistic aberration and Faraday rotation (Lyutikov, Pariev, & Gabuzda 2005), the EVPA should be aligned predominantly perpendicular to the projection of the magnetic field onto the plane of the sky. Therefore, increased polarization towards the edges of the jet, with EVPA aligned roughly perpendicular to the jet axis, presents a polarimetric signature of a jet sheath. This signal was detected in the stacked radio map of PKS 1510–089.

In this paper, we extend our modeling of orphan γ -ray flares and analysis of radio maps to a larger sample of blazars. In particular, we search for orphan γ -ray flares in a sample of blazars monitored by the BU blazar group: www.bu.edu/blazars/VLBaproject.html. We calculate γ -ray light curves using data provided by the Fermi Gamma-ray Space Telescope and construct optical light curves in R band using ground based telescopes around the world (for details see Williamson et al. 2014). We define an orphan γ -ray flare as a γ -ray flare that does not have an optical counterpart.

TABLE 1
RING OF FIRE GLOBAL PARAMETERS

Electron Power-Law Parameters	Value
γ_{\min}	2.0×10^3
γ_{\max}	1.0×10^4
s	4.0
Blob Parameters	Value
r_{blob}	0.09 (pc)
B_{blob}	0.02 (G)
Ring Parameters	Value
r_{\min}	0.09 (pc)
r_{\max}	0.18 (pc)
h_o	0.018 (pc)
B_{ring}	0.12 (G)

This paper is organized as follows: In §2 we summarize the *Ring of Fire* model and outline the model parameters (a detailed description of which can be found in MacDonald et al. 2015). In §3 we describe our method of radio map stacking. In §4 we present our stacked radio maps and orphan γ -ray flare models for our sample of blazars. §5 contains our summary and conclusions. We adopt the following cosmological parameters: $H_o = 70 \text{ km s}^{-1} \text{ Mpc}^{-1}$, $\Omega_m = 0.3$, and $\Omega_\Lambda = 0.7$.

2. THE RING OF FIRE MODEL

The *Ring of Fire* model incorporates two blazar emission zones. The two zones interact radiatively through inverse-Compton scattering. The ring supplies a source of seed photons that are up-scattered to γ -ray energies by a power-law distribution of electrons contained within the blob. The electron power-law energy distribution (both in the ring and in the blob) is set to $n_e(\gamma) \propto \gamma^{-s}$,

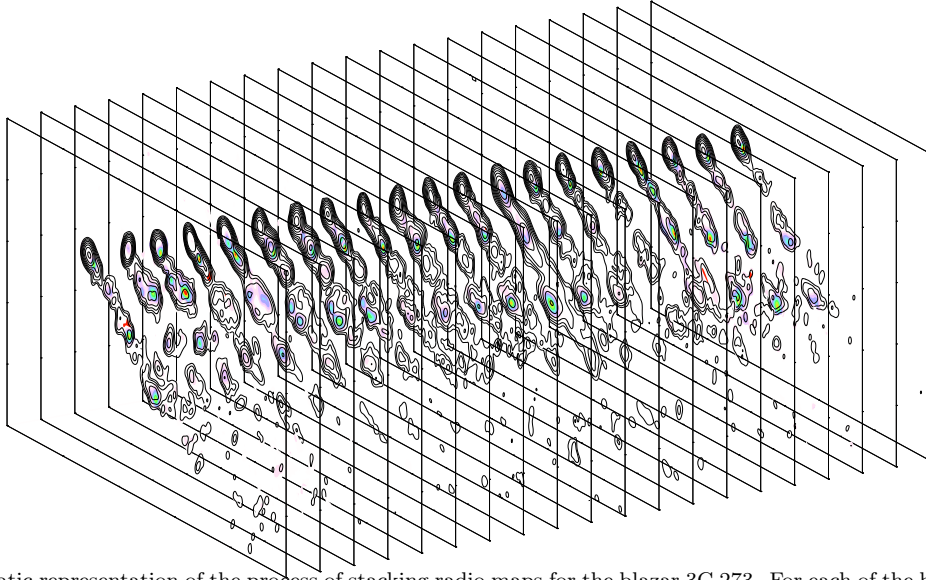


FIG. 2.— A schematic representation of the process of stacking radio maps for the blazar 3C 273. For each of the blazars in our sample, we selected roughly twenty epochs of relatively quiescent jet activity. The VLBA data were obtained from 2008 to 2016 as part of the VLBA-BU-BLAZAR program (see www.bu.edu/blazars/VLBAproject.html and Jorstad et al. (2013) for a general description of the observations and data analysis). For each epoch we used Difmap’s *modelfit* task to locate the radio core. The images were then aligned (based on the location of the radio core) and added together to create stacked I, Q, and U maps (shown in Figure 3).

over the energy range γ_{\min} to γ_{\max} , where the energy of a given electron is $E = \gamma m_e c^2$. The emission is computed in the co-moving frame of the blob, after which a series of Lorentz transformations is applied to obtain the flux in the observer’s frame. In particular, we compute three different photon production rates accounting for synchrotron and synchrotron self-Compton photons produced internally to the blob and external Compton photons produced by the blob’s passage through the photon field of the ring. The distribution of electrons in the blob is evolved each time step by solving the Fokker-Planck equation (Kardashev 1962), thus accounting for radiative losses as the blob propagates through the ring. We include an injection power (P_{inj}) that parameterizes a physical mechanism at work within the blob (e.g., turbulence or diffusive shock acceleration), which continuously rejuvenates the aging blob electron distribution. The blob is assumed to be spherical with a radius r_{blob} . The ring of shocked sheath is parameterized by an inner (r_{\min}) and outer (r_{\max}) radius and a thickness (h_o). Uniform magnetic fields are set in the blob (B_{blob}) and in the ring (B_{ring}), both of which are assumed constant over the time it takes the blob to pass through the ring. The blob begins its acceleration towards the ring at z_{initial} (along the jet axis) with an initial bulk Lorentz factor Γ_{initial} ($v_{\text{blob}} \equiv c \sqrt{1 - \Gamma^{-2}}$). The blob ceases its acceleration at z_{final} after which it continues down the jet at a constant speed of Γ_{final} . The ring is situated at $z_{\text{ring}} = 0$ pc (the origin of our model), and although in reality the sheath (and by extension our ring) will have some velocity parallel to the jet spine, for the purposes of this calculation the ring is treated as static. Finally, we include a baseline level of flux in the optical (Baseline Flux_{optical}) and γ -ray (Baseline Flux _{γ -ray}) bands, to which the variable emission produced by our model is added. These baseline fluxes mirror the more slowly varying flux of the jet and are assumed to be constant over the course of our

simulations. The parameters Γ_{initial} , Γ_{final} , z_{initial} , z_{final} , P_{inj} , the baseline fluxes, the angle of inclination of the jet to our line-of-sight (θ_{obs}), and the redshift (Z) are all source/flare specific and are listed in Table 2 for each source considered. The rest of the model parameters are fixed for all of the calculations presented below, and their specific values are listed in Table 1. For a more in-depth description of the physics included in these calculations, see MacDonald et al. (2015).

3. RADIO MAP STACKING

In order to detect the faint polarimetric signature of a jet sheath, we implement a method of radio map stacking (see, e.g., Fromm et al. 2013; Zamaninasab et al. 2013). For each blazar in our sample, we stack roughly twenty radio images obtained at a frequency of 43 GHz with the Very Long Baseline Array (VLBA) as part of the VLBA-BU-BLAZAR program (see www.bu.edu/blazars/VLBAproject.html). In particular, we selected epochs from relatively quiescent periods of jet activity. The aim of stacking the images is to “smooth” out transient features (like blobs propagating down the jet) and to “amplify” more static structures in the jet (like a jet sheath). Each image is carefully aligned within the stack based on the location of the radio core at 43 GHz. At the majority of our epochs, the radio core is the brightest feature in the jet; however, there are epochs where the flux from a blob downstream exceeds that of the radio core. In order to avoid misidentification of the radio cores at the various epochs included in our stacked maps, we use the Difmap procedure *modelfit* to identify the core among the features in each radio map. We then use an IDL code to align and stack the images (see Figure 2) based on the location of the radio core in each image. By stacking these images we are able to build up a radio signal from the periphery of each jet in our sample where the plasma sheath is hypothesized to exist.

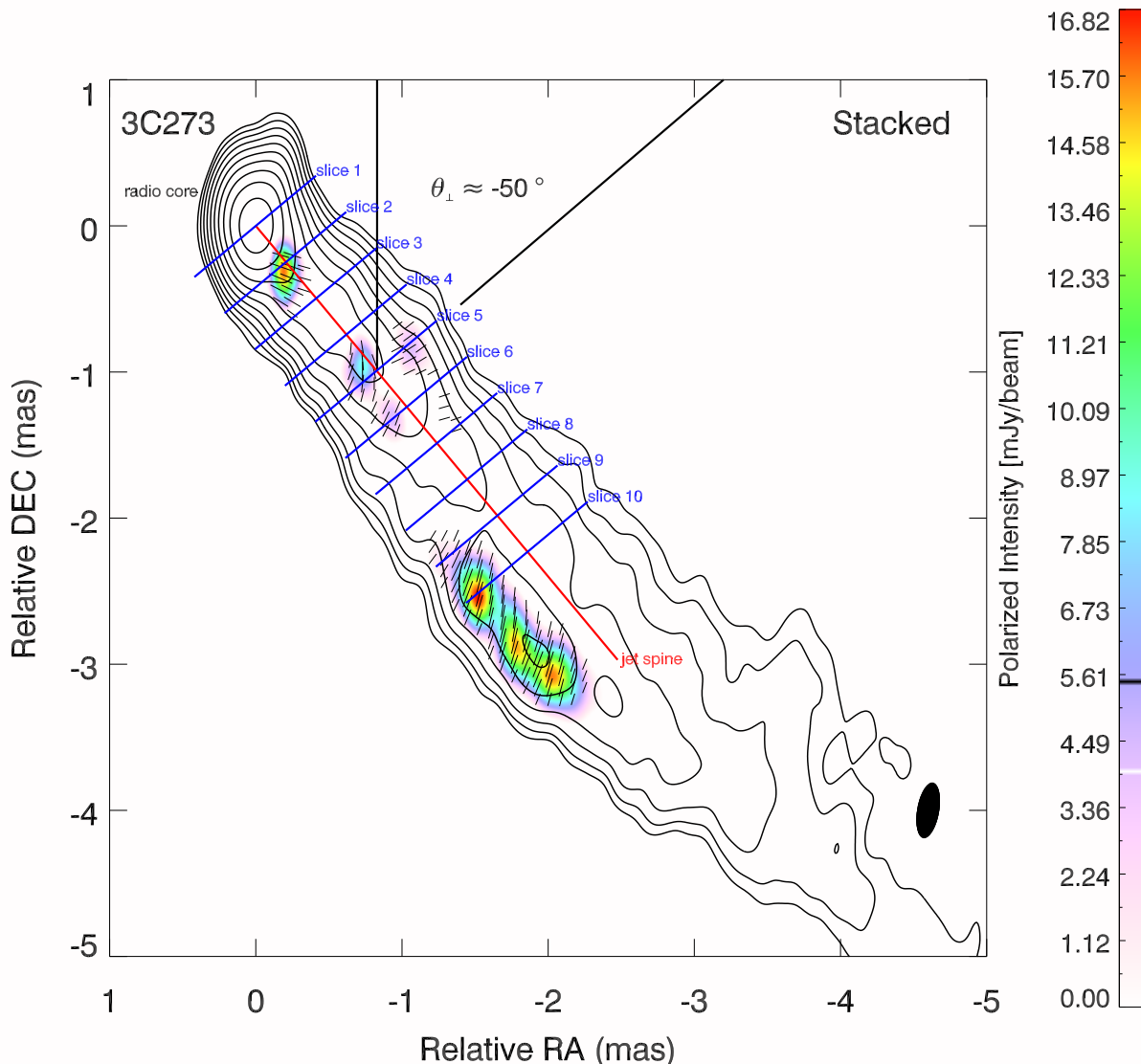


FIG. 3.— A stacked map of 43 GHz images of 3C 273 spanning twenty epochs of observation from 2008 to 2016. The black contours correspond to total intensity (contour levels are: 3.8, 7.5, 15.0, 30.0, 60.1, 120.2, 240.5, 480.9, 961.9, 1923.9 mJy beam⁻¹), whereas the underlying color scheme corresponds to polarized intensity (see color bar to the right for the flux levels), with the EVPAs denoted by black line segments. The EVPAs indicate the orientation of linear polarization as projected onto the plane of the sky. All images have been convolved with a Gaussian beam, shown in the bottom right corner of the stacked map. A jet spine is plotted in red based on the transverse symmetry of the jet, across which ten transverse slices through the data are taken (shown in blue). The profiles of the emission parameters along the fifth slice are shown in Figure 5. The two black lines highlight the angle (θ_{\perp}) between 0° (i.e. North) and 90° relative to the jet spine (in red) for the fifth slice. This transverse orientation relative to the jet spine is plotted as a horizontal black line in Figure 5 to highlight EVPAs that are oriented roughly perpendicular to the jet axis.

4. RESULTS

4.1. 3C 273

For an initial test of our stacking procedure’s ability to detect jet sheaths, we selected the blazar 3C 273. At a redshift of $Z = 0.158$ (Lavaux & Hudson 2011), 3C 273 is one of the closest examples of a blazar, and as such is an ideal candidate to search for a jet sheath. As outlined in §3, we selected twenty relatively quiescent epochs of

jet activity to create the stacked radio map shown in Figure 3. As predicted by the spine-sheath model, the linear polarization increases toward the edges of the jet downstream of the radio core. The EVPAs downstream are predominantly inclined to the jet spine (shown as a red line delineating the historical trajectories taken by blobs ejected from the radio core). A series of slices was taken through our stacked map to highlight the profiles of the Stokes parameters transverse to the jet axis.

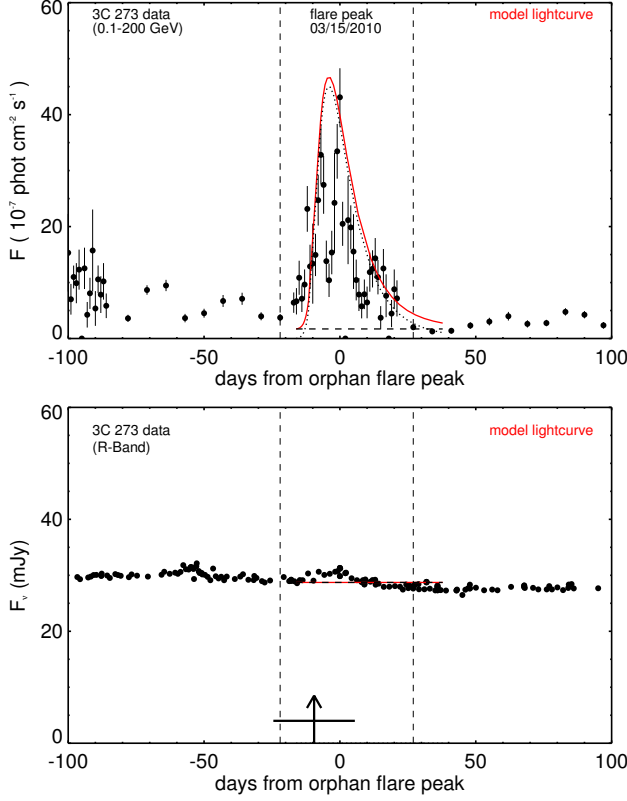


FIG. 4.— Light curves of 3C 273 (black circles) in the γ -rays (upper panel) and optical (lower panel). The model light curves are overlaid in red and consist of the superposition of the model baseline level of flux in each band (the horizontal dashed black line) and the variable emission produced by the model (the dotted black line). The vertical arrow in the lower panel marks the time when a superluminal knot passed through the 43 GHz core of 3C 273, with the horizontal bar representing the uncertainty in this time.

We detect an orphan γ -ray flare in the Fermi LAT light curve during March 2010. The corresponding light curves in γ -rays and in the optical band are shown in Figure 4. The VLBA images also exhibit the ejection of a blob from the radio core of 3C 273 during the onset of this orphan flare on March 6th 2010 \pm 25 days (Jorstad et al. 2017, in prep.), with a bulk Lorentz factor of $\Gamma \sim 6$. The time of the blob ejection is demarcated by a vertical arrow in the lower panel of Figure 4. Table 2 lists the *Ring of Fire* model parameters used to obtain a fit to this orphan γ -ray flare. The synthetic γ -ray and optical light curves produced by the *Ring of Fire* model are overlaid in red. The general strategy used to fit the orphan flares presented within this paper was to start with the parameters used in MacDonald et al. (2015) to model the orphan γ -ray flare from PKS 1510–089. As discussed in MacDonald et al. (2015), the shape of the orphan flare profile produced by the *Ring of Fire* model is very sensitive to the nature of the blob’s acceleration down the jet spine. With this in mind, the ring parameters were held constant and only the nature of the blob’s acceleration was modified to obtain the above fit to the data. Due to the larger inclination angle of the jet in 3C 273 to our line of sight ($\theta_{\text{obs}} = 6.1^\circ$ in contrast to PKS 1510–089 where $\theta_{\text{obs}} = 1.4^\circ$; Jorstad et al. 2005), the power (P_{inj}) injected into the blob was also increased in order to match the observed flux levels. The bulk Lorentz factor used in our model ($\Gamma \sim 25$) is much larger than the

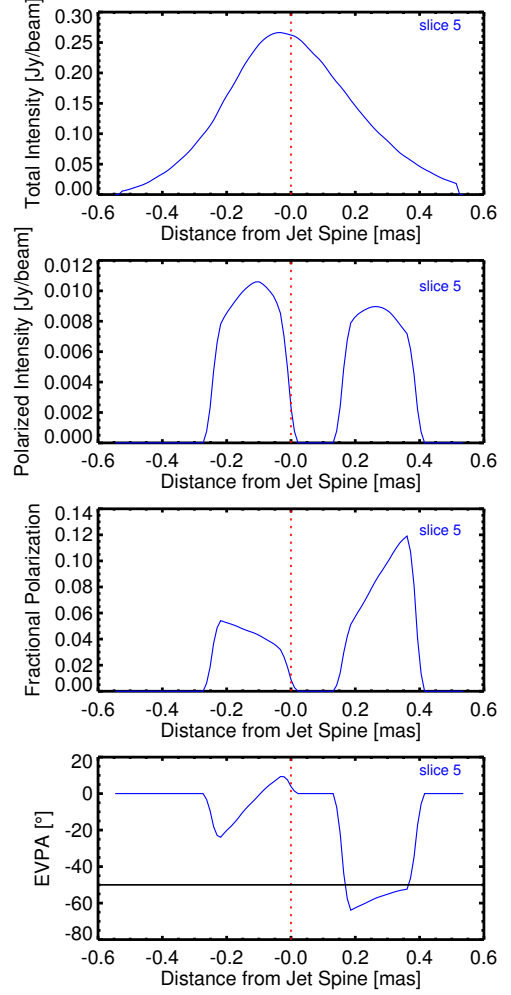


FIG. 5.— Variations of the emission parameters of 3C 273 transverse to the jet axis (dashed red line) for slice 5 (shown in Figure 3) from top to bottom: total intensity, polarized intensity, fractional polarization, and EVPA. The fractional polarization increasing toward the edges of the jet is a predicted polarimetric signature of a jet sheath (as discussed in §1), with the EVPA transverse to the axis. The black line in the lower panel delineates EVPAs that are exactly \perp to the jet spine.

apparent speed of the knot above. The disparity in these values highlights either (i) a shortcoming in our model or (ii) some form of (de)acceleration experienced by the blob upstream of the core (see, e.g., Georganopoulos & Kazanas 2003).

Figure 5 shows the profiles of the Stokes parameters (I, Q, and U) transverse to the jet axis along the fifth slice through our stacked map (Figure 3). The upper middle panel highlights the double peaked profile in the linearly polarized intensity ($\sqrt{Q^2 + U^2}$). The lower middle panel shows how the fractional polarization ($\sqrt{Q^2 + U^2}/I$) increases towards the edges of the jet, in agreement with the spine-sheath model. It should be noted that there is a polarized feature just downstream of the radio core in our stacked map (Figure 3, slice 2) with EVPAs aligned parallel to the jet spine. This is a signature expected for a standing shock just downstream of the radio core that compresses and aligns the magnetic field (Cawthorne & Cobb 1990).

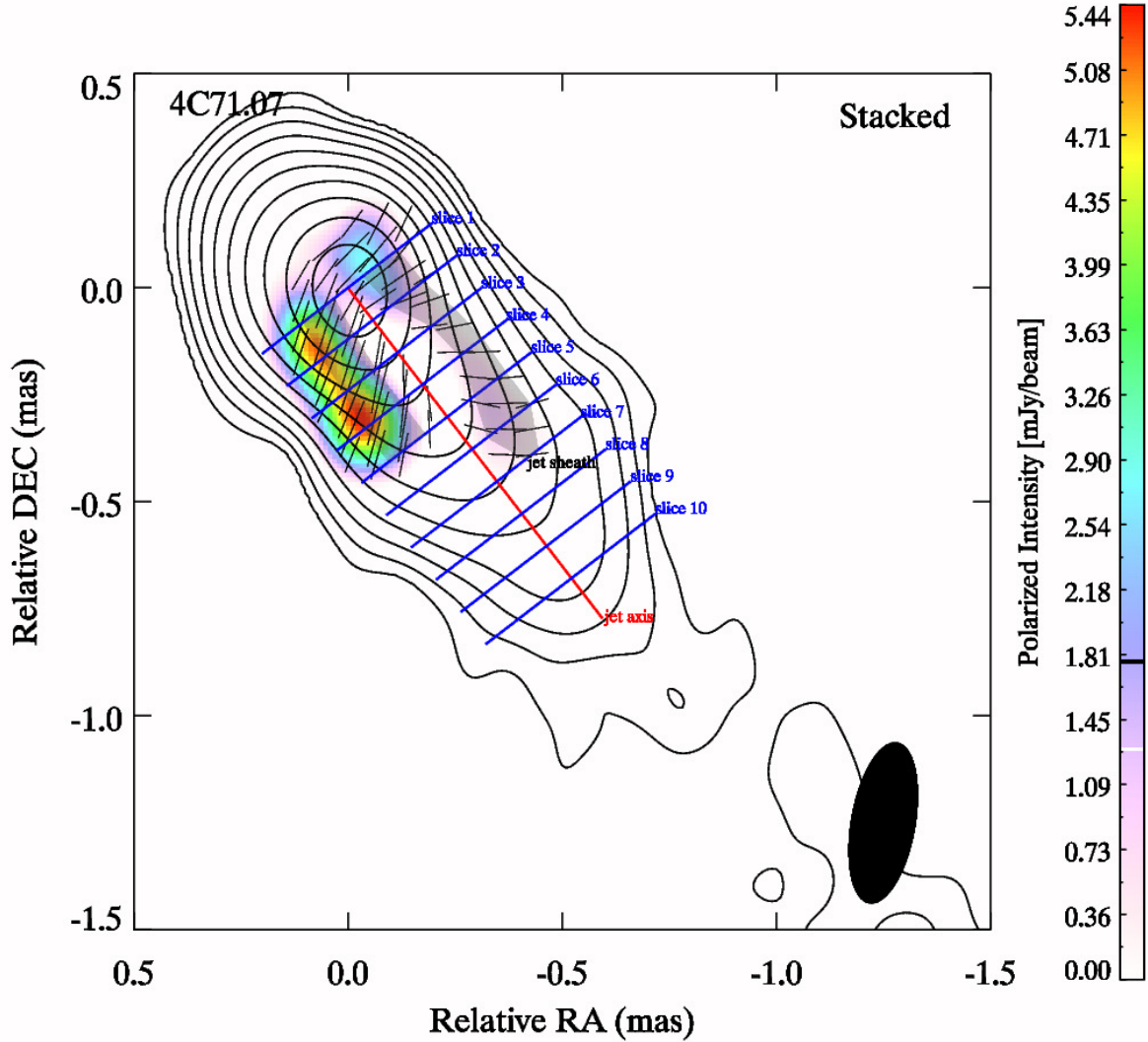


FIG. 6.— A stacked map of 43 GHz images of 4C 71.07 spanning twenty epochs of observation from 2008 to 2016. As in Figure 3, the black contours correspond to total intensity (contour levels are: 0.9, 1.9, 3.9, 7.9, 15.8, 31.7, 63.4, 126.9, 253.9, 507.8 mJy beam⁻¹), whereas the underlying color scheme corresponds to polarized intensity (see color bar to the right for the flux levels), with the EVPAs denoted by black line segments. The EVPAs indicate the orientation of linear polarization as projected onto the plane of the sky. All images have been convolved with a Gaussian beam, shown in the bottom right corner of the stacked map. A jet spine is plotted in red based on the transverse symmetry of the jet, across which ten transverse slices through the data are taken (shown in blue). The profiles of the emission parameters along the first slice are shown in Figure 8. The shaded gray regions in the above map highlight the nominal location of the jet sheath of 4C 71.07 as determined by the procedure illustrated in Figure 9.

4.2. 4C 71.07

Figure 6 presents a stacked radio map of the blazar 4C 71.07 (0836+710). A very prominent and continuous polarimetric signature of a jet sheath is evident down the edges of the jet in this stacked radio image. Given the continuous nature of the jet sheath on the image, we can estimate the bolometric luminosity of the sheath. This is accomplished by first using the extent of the polarized intensity profile along each of the slices to trace out the shaded gray regions shown in Figure 9 (see also Figure 6). The width of the sheath on each side of the slice is determined, arbitrarily, by the location where the polarized

flux falls below 0.85 times the peak value. An estimate of the bolometric luminosity (L_{bol}) of the sheath is computed by adding all of the flux contained within the gray shaded regions of our stacked map. We convert this inferred sheath flux at 43 GHz into a spectral luminosity and assume a power-law ($L_{\nu} \propto \nu^{-\alpha}$), which we then integrate over a range of frequencies that encompass the sheath's radiation to obtain:

$$L_{\text{bol}} = \int_{\nu_{\min}}^{\nu_{\max}} L_{\nu} d\nu \sim 1 \times 10^{44} \text{ erg s}^{-1}, \quad (1)$$

where we have assumed a spectral index of $\alpha \sim 1.0$ and limits of integration of $\nu_{\min} = 10^9$ Hz and $\nu_{\max} = 5 \times$

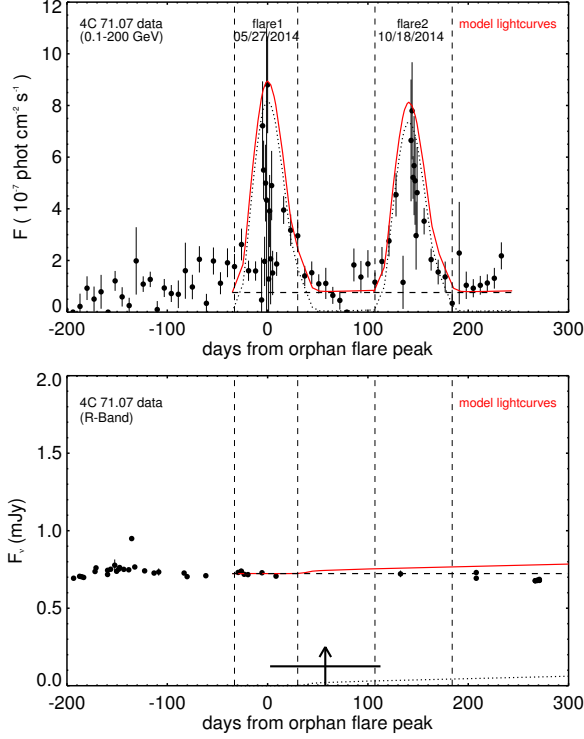


FIG. 7.— Light curves of 4C 71.07 (black circles) in the γ -rays (upper panel) and optical (lower panel). The model light curves are overlaid in red and consist of the superposition of the model baseline level of flux in each band (the horizontal dashed black line) and the variable emission produced by the model (the dotted black line). The vertical arrow in the lower panel marks the time when a superluminal knot passed through the 43 GHz core of 4C 71.07, with the horizontal bar representing the uncertainty in this time.

10^{13} Hz. Our estimate indicates that the jet sheath is an important source of seed photons even at parsec scales. An estimate of the inner (r_{\min}) and outer (r_{\max}) radii of the sheath was made by averaging the values obtained for these parameters relative to the jet spine for each slice through the stacked map. We find that $r_{\min} \sim 0.27$ pc and $r_{\max} \sim 0.34$ pc. These values are larger than the inner and outer radii used in our model of the ring (see Table 1) that we posit to exist upstream of the radio core.

We detect two orphan γ -ray flares in the Fermi LAT light curve of 4C 71.07 during 2014 (Figure 7), although the optical observations are sparse. The first orphan flare occurred in May followed by a second in October. Table 2 lists the *Ring of Fire* model parameters used to obtain a fit to this pair of orphan flares. For this particular case, two consecutive blobs were launched through the ring of shocked sheath. The nature of the blob acceleration down the jet spine was identical for the two blobs, with the only difference being a slightly smaller injection power used in the passage of the second blob through the ring. The VLBA monitoring indicates the ejection of a blob from the 43 GHz core of 4C 71.07 on July 24th 2014 ± 55 days (Jorstad - private communication) with a bulk Lorentz factor of $\Gamma \sim 32$. The bulk Lorentz factor in our model ($\Gamma \sim 10$) is too low compared to this VLBI speed. Again, as in the case of 3C 273, this discrepancy potentially highlights some form of acceleration occurring within the jet (see, e.g., Marscher et al. 2008, Homan et al. 2015).

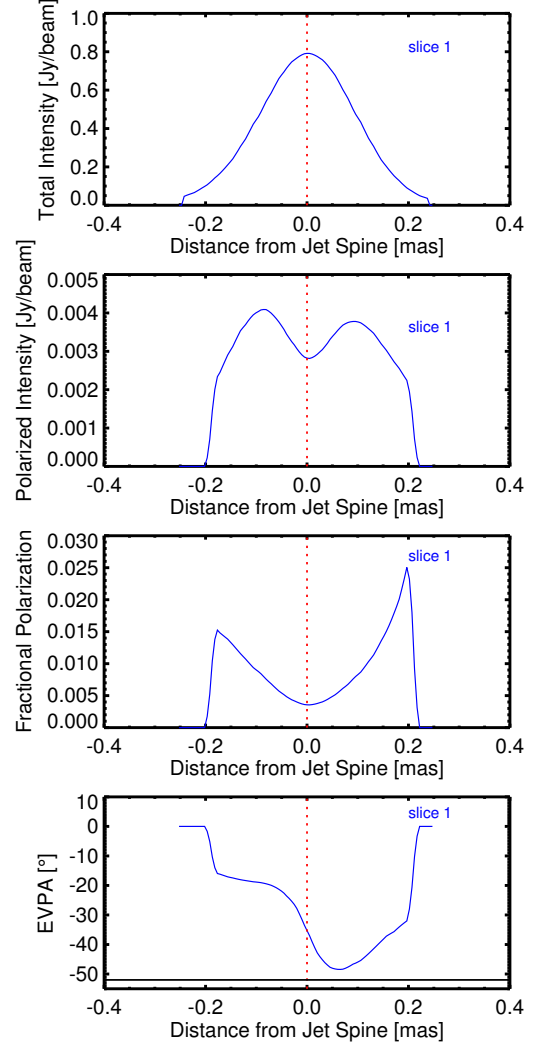


FIG. 8.— Variations of the emission parameters transverse to the jet axis (dashed red line) of 4C 71.07 for slice 1 (shown in Figure 6) from top to bottom: total intensity, polarized intensity, fractional polarization, and EVPA. The fractional polarization increasing toward the edges of the jet is a predicted polarimetric signature of a jet sheath (as discussed in §1), with the EVPA transverse to the axis. The black line in the lower panel delineates EVPAs that are exactly \perp to the jet spine.

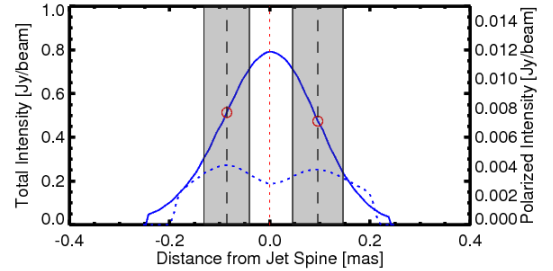


FIG. 9.— The polarized intensity profile of 4C 71.07 along slice 1 (dashed blue line corresponding to the right-hand axis) is overlaid upon the total intensity profile for slice 1 (solid blue line corresponding to the left-hand axis). We use this double-peaked profile to highlight the likely location of the sheath within each slice (shaded gray regions). The sheath's contribution to the jet's total intensity profile is estimated by the values of total intensity (red circles) that are cospatial with the peaks of the polarized intensity profile (demarcated by dashed vertical lines). This procedure is then repeated for each slice, thus tracing out the sheath (shaded gray regions) shown in Figure 6.

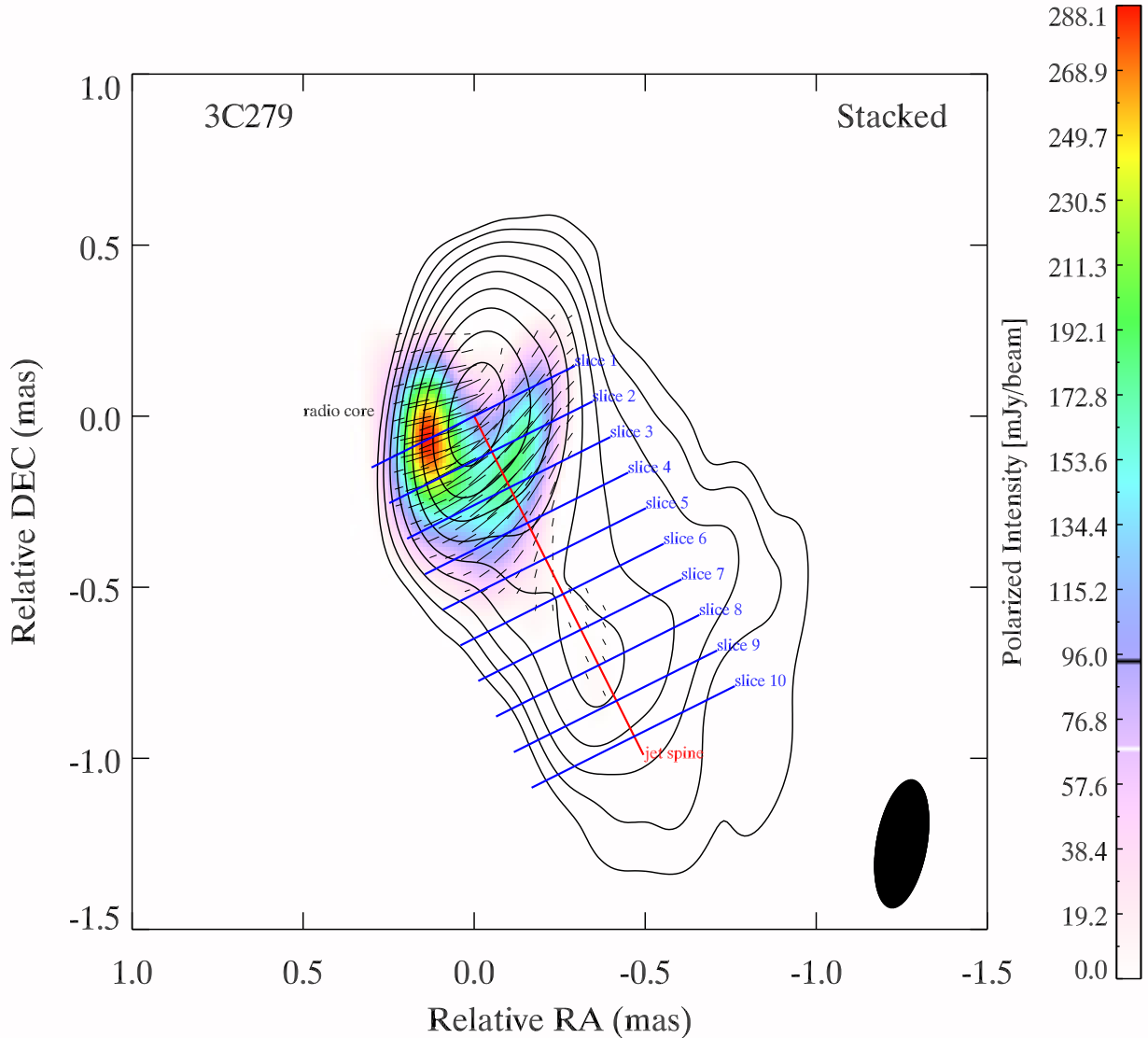


FIG. 10.— A stacked map of 43 GHz images of 3C 279 spanning ten epochs of observation from 2008 to 2016. The black contours correspond to total intensity (contour levels are: 20.5, 41.0, 82.0, 164.0, 328.0, 656.1, 1312.2, 2624.4, 5248.9 mJy beam⁻¹), whereas the underlying color scheme corresponds to polarized intensity (see color bar to the right for the flux levels), with the EVPAs denoted by black line segments. The EVPAs indicate the orientation of linear polarization as projected onto the plane of the sky. All images have been convolved with a Gaussian beam, shown in the bottom right corner of the stacked map. A jet spine is plotted in red based on the transverse symmetry of the jet, across which ten transverse slices through the data are taken (shown in blue). The profiles of the emission parameters along the first slice are shown in Figure 12.

4.3. 3C 279

In Figure 10 we present a stacked radio map of the blazar 3C 279. In contrast to the stacked radio maps of 3C 273 (Figure 3) and 4C 71.07 (Figure 6), our map of 3C 279 shows a far more complex polarimetric pattern down the length of the jet. Initially, the EVPAs are aligned perpendicular to the jet axis in the vicinity of the radio core. The polarization then bifurcates across the width of the jet, with the EVPAs remaining inclined predominantly perpendicular to the jet axis (especially

on the edges of the jet). The linearly polarized intensity, however, peaks to one side of the jet (see the upper middle panel of Figure 12, in which the “double-peaked” linearly polarized intensity profile is not as symmetric as those shown in Figures 5 & 8). Farther downstream the EVPAs align with the jet axis and the polarization becomes confined to the jet spine.

An orphan γ -ray flare with no similar optical counterpart is seen in the Fermi LAT light curve of 3C 279 during April 2014. The corresponding γ -ray and optical light curves are shown in Figure 11. Table 2 lists the *Ring*

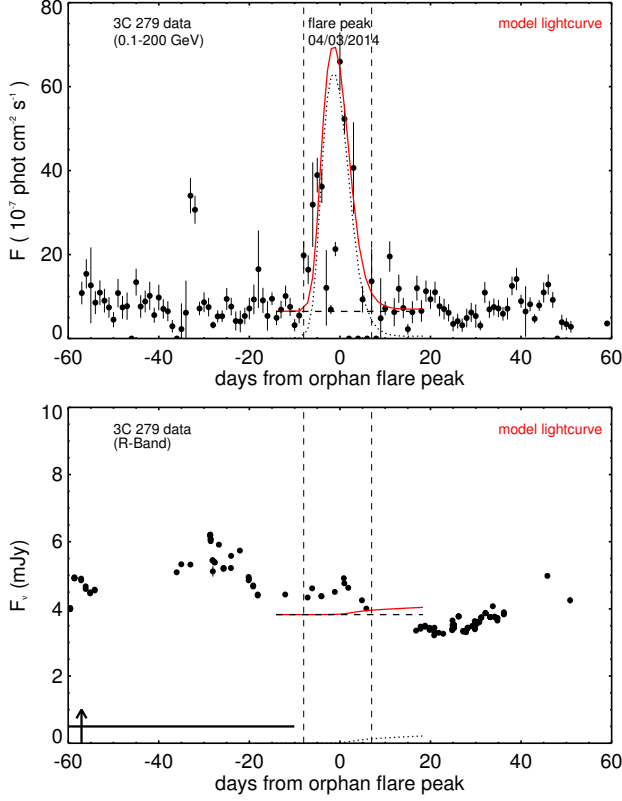


FIG. 11.— Light curves of 3C 279 (black circles) in the γ -rays (upper panel) and optical (lower panel). The model light curves are overlaid in red and consist of the superposition of the model baseline level of flux in each band (the horizontal dashed black line) and the variable emission produced by the model (the dotted black line). The vertical arrow in the lower panel marks the time when a superluminal knot passed through the 43 GHz core of 3C 279, with the horizontal bar representing the uncertainty in this time.

of *Fire* model parameters used to obtain a fit to this orphan γ -ray flare. Again, the synthetic γ -ray and optical light curves produced by the *Ring of Fire* model are overlaid in red. There are several statistically significant data points in the γ -ray flare profile that are not reproduced by the *Ring of Fire* model. These three data points occur shortly after the onset of the orphan flare and result in a “kink” in the flare profile. This kink could represent some catastrophic loss of electrons within the blob, perhaps as the relativistic electron injection mechanism at work within the blob (e.g., turbulence or magnetic reconnection) momentarily ceases. This type of short-term discontinuity in the flare profile is not accounted for in the *Ring of Fire* model, in which the internal conditions within the blob remain fixed over the course of the blob’s passage through the ring of shocked sheath.

The linearly polarized intensity present in our stacked radio map highlights the complex nature of the magnetized plasma within 3C 279 on parsec scales. The observed peak in the polarized intensity (located to the left of the jet axis in Figure 10) may be associated with a standing feature within the jet downstream of the radio core. This feature might represent a “bend” in the jet, which would create a localized “hot spot” resulting from a standing oblique shock that deflects the radio jet as it encounters the surrounding ambient medium. The fact that the polarimetric signature of the sheath is confined to such a small region is encouraging from

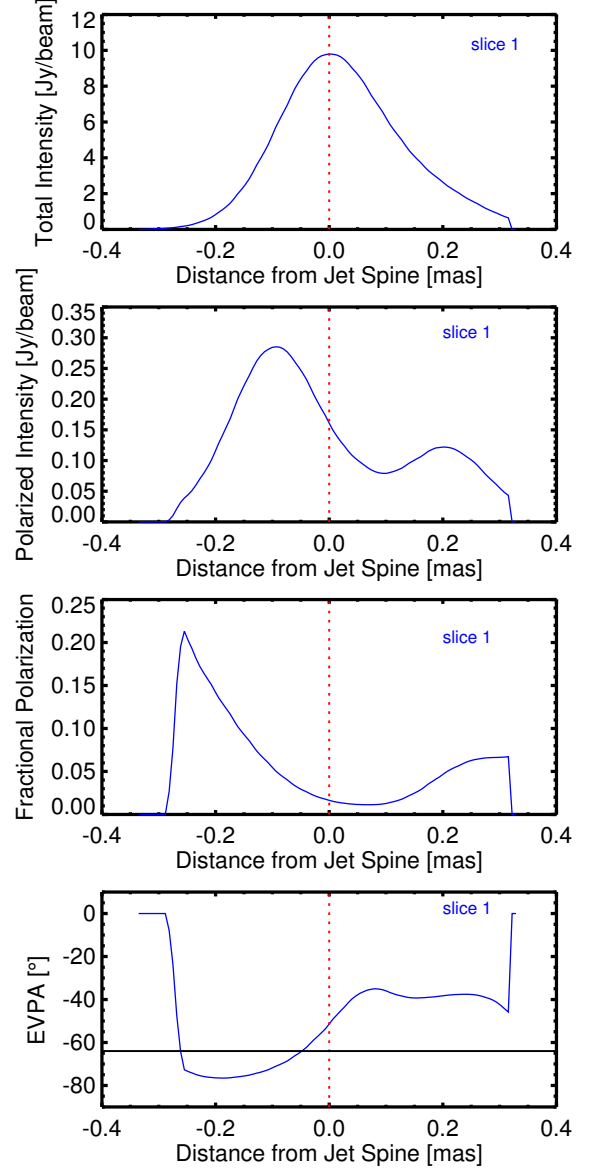


FIG. 12.— Variations of the emission parameters of 3C 279 transverse to the jet axis (dashed red line) for slice 1 (shown in Figure 10) from top to bottom: total intensity, polarized intensity, fractional polarization, and EVPA. The fractional polarization increasing toward the edges of the jet is a predicted polarimetric signature of a jet sheath (as discussed in §1), with the EVPA transverse to the axis. The black line in the lower panel delineates EVPAs that are exactly \perp to the jet spine.

a modeling standpoint. The *Ring of Fire* model would predict that, as a blob propagates through this particular region within 3C 279, one might expect to observe an orphan flare due to the inverse-Compton scattering of this segment of sheath’s photons off of the blob’s electrons. The VLBA-BU-Blazar program detected the ejection of a blob 57 ± 47 days before this orphan flare with a bulk Lorentz factor of $\Gamma \sim 21$ (Jorstad - private communication). Perhaps the orphan flare in Figure 11 is associated with this blob as it propagates through the sheath region highlighted downstream of the core in Figure 10. A second blob was also detected 196 ± 33 days after this flare with a bulk Lorentz factor of $\Gamma \sim 31$.

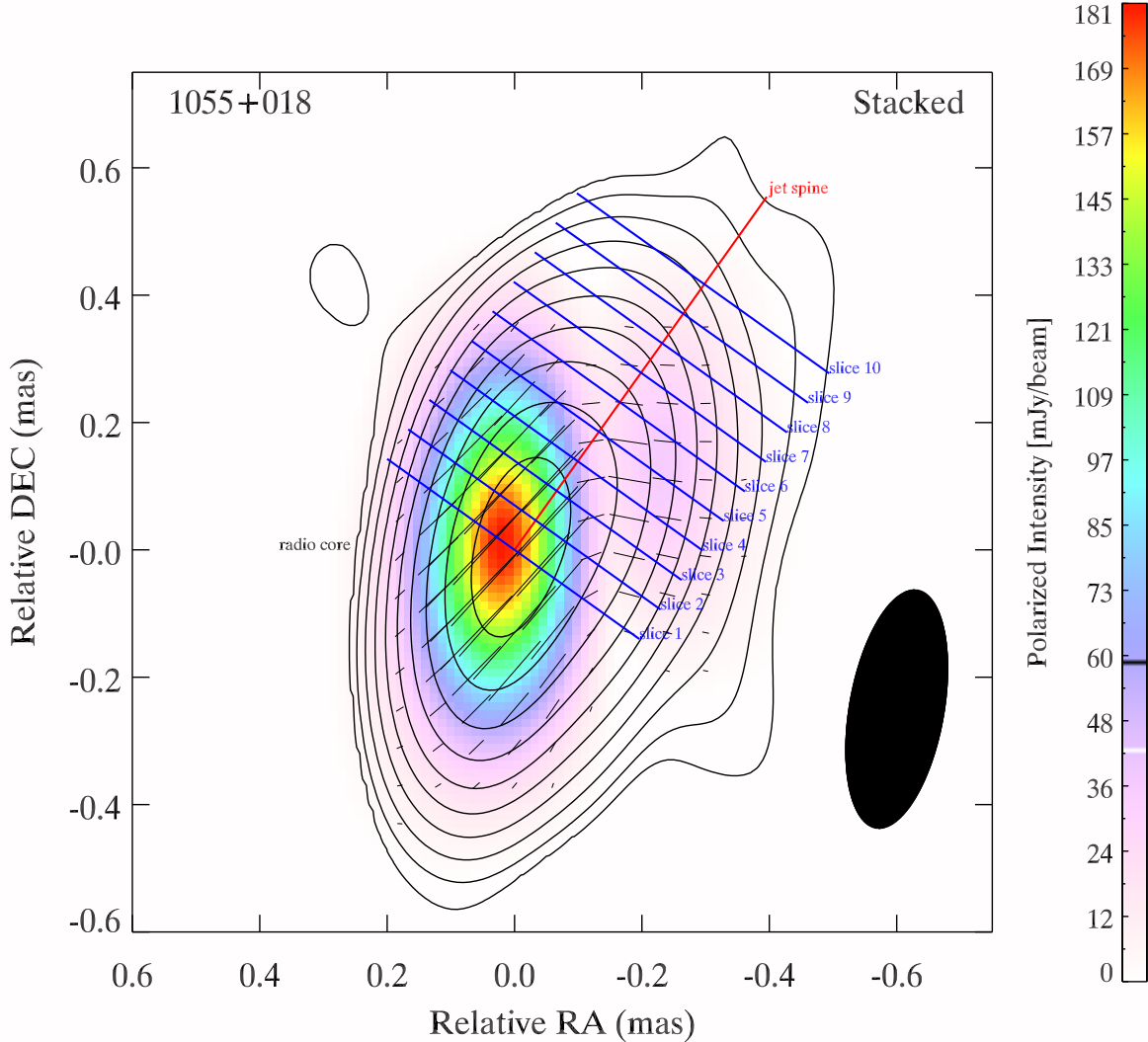


FIG. 13.— A stacked map of 43 GHz images of 1055+018 spanning twenty epochs of observation from 2008 to 2016. The black contours correspond to total intensity (contour levels are: 2.8, 5.7, 11.4, 22.9, 45.8, 91.6, 183.3, 366.7, 733.4, 1466.9 mJy beam⁻¹), whereas the underlying color scheme corresponds to polarized intensity (see color bar to the right for the flux levels), with the EVPAs denoted by black line segments. The EVPAs indicate the orientation of linear polarization as projected onto the plane of the sky. All images have been convolved with a Gaussian beam, shown in the bottom right corner of the stacked map. A jet spine is plotted in red based on the transverse symmetry of the jet, across which ten transverse slices through the data are taken (shown in blue). The profiles of the emission parameters along the third slice are shown in Figure 15.

4.4. 1055+018

Figure 13 illustrates a stacked radio map of the blazar 1055+018. In this stacked map the peak of the polarized intensity is co-spatial with the radio core. The EVPAs within the radio core are roughly aligned with the axis of the jet (in red) indicative of shock acceleration compressing and aligning the magnetic field perpendicular to the jet flow. Slightly downstream of the polarized emission in the core is a second polarimetric feature on the edge of the jet (to the west). Within this second feature the EVPAs are inclined to the jet axis shown in red. This feature is not mirrored on the other side of the jet as in the map of 4C 71.07 (Figure 6). The sheath polarization

that we do detect is probably Doppler beamed to some extent. It is possible that there is a sheath located on the far side of the jet (to the east) that is undetected due to weaker Doppler beaming as a result of jet orientation.

The Fermi LAT detected an orphan γ -ray flare with no optical counterpart in 1055+018 during February 2014. The corresponding γ -ray and optical light curves are shown in Figure 14. Table 2 lists the *Ring of Fire* model parameters used to obtain a fit to this orphan γ -ray flare, with the model light curves overlaid in red. The nature of the blob's acceleration was adjusted until a fit to this asymmetric orphan flare profile (with a more gradual flare onset and a steeper flare decay) was obtained.

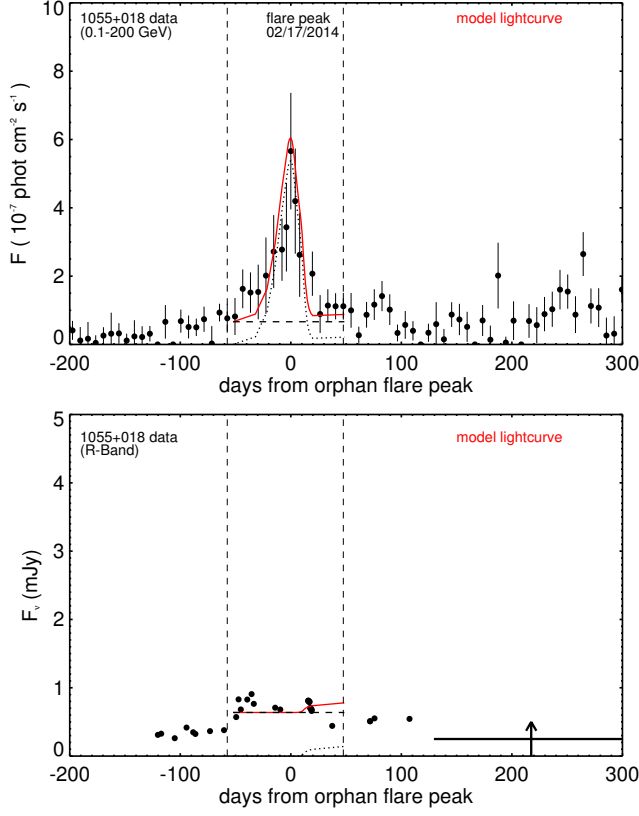


FIG. 14.— Light curves of 1055+018 (black circles) in the γ -rays (upper panel) and optical (lower panel). The model light curves are overlaid in red and consist of the superposition of the model baseline level of flux in each band (the horizontal dashed black line) and the variable emission produced by the model (the dotted black line). The vertical arrow in the lower panel marks the time when a superluminal knot passed through the 43 GHz core of 1055+018, with the horizontal bar representing the uncertainty in this time.

As with the other orphan flare models presented in this paper, the ring parameters were held constant and the blob's injection power was altered to fit the corresponding level of flux. There is a slight “bump” in the synthetic optical light curve due to the Doppler boost of the emission gained from the blob's acceleration down the jet spine. The synchrotron emission in the co-moving frame of the blob, however, remains constant due to the fixed nature of the magnetic field within the blob during the simulation. The VLBA-BU-Blazar program detected the ejection of a blob from the radio core of 1055+018 214 ± 88 days after this flare with a bulk Lorentz factor of $\Gamma \sim 15$ (Jorstad - private communication). This VLBI speed is similar to our model value of $\Gamma_{\text{final}} \sim 20$ (see Table 2). The *Ring of Fire* posits that the site of orphan γ -ray flare production is located upstream of the radio core. Our model, therefore, predicts that one should indeed see radio blobs pass through the 43 GHz core after the occurrence of an orphan flare.

The profiles of the Stokes emission parameters transverse to the jet axis along the third slice through our stacked map of 1055+018 are shown in Figure 15. The increase in fractional linear polarization towards the edges of the jet is clearly visible in the lower middle panel. The linearly polarized intensity profile (upper middle panel) is asymmetric across the jet axis. It should be pointed out that an alternate interpretation of the polarimetric

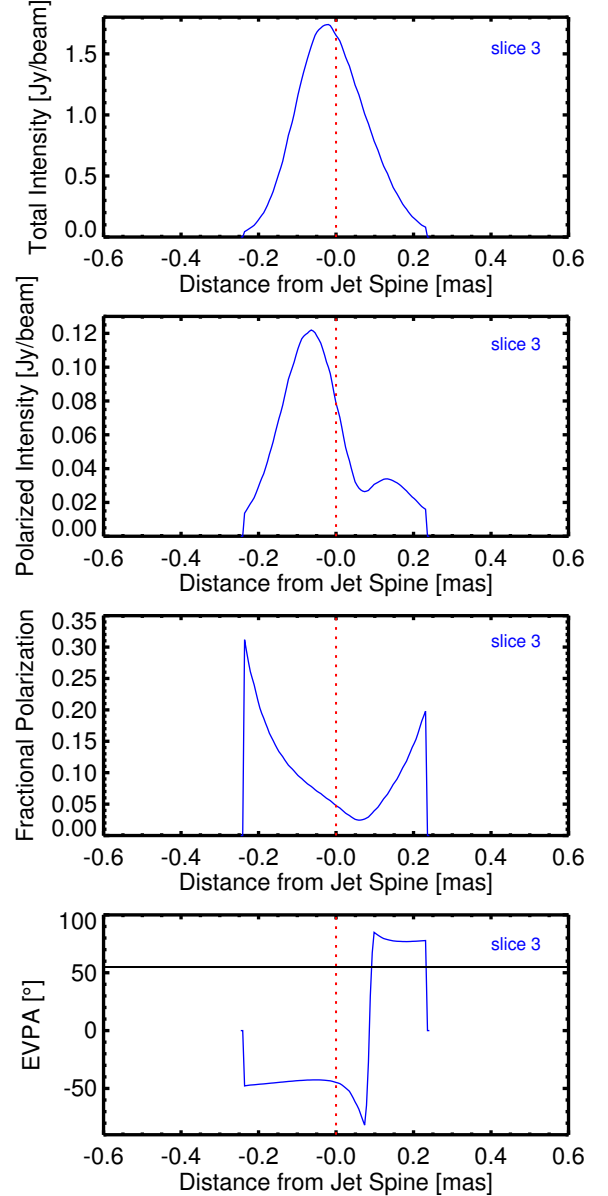


FIG. 15.— Variations of the emission parameters of 1055+018 transverse to the jet axis (dashed red line) for slice 3 (shown in Figure 13) from top to bottom: total intensity, polarized intensity, fractional polarization, and EVPA. The fractional polarization increasing toward the edges of the jet is a predicted polarimetric signature of a jet sheath (as discussed in §1), with the EVPA transverse to the axis. The black line in the lower panel delineates EVPAs that are exactly \perp to the jet spine.

profiles presented in Figure 15 (and indeed the rest of the profiles presented in this paper) is that, in contrast to the spine-sheath model, the jet carries a large scale helical magnetic field (see, e.g., Gabuzda, Reichstein, & O'Neill 2013). A determination of the rotation measure (RM) across the width of the jet can, in theory, distinguish between these two scenarios. We adopt the spine-sheath interpretation in this paper. Regardless of whether the polarization that we detect emanates from a jet sheath or a large scale helical magnetic field, this polarization does delineate a distinct region of magnetized plasma within the jet that will produce a localized source of seed photons (required by the *Ring of Fire* model).

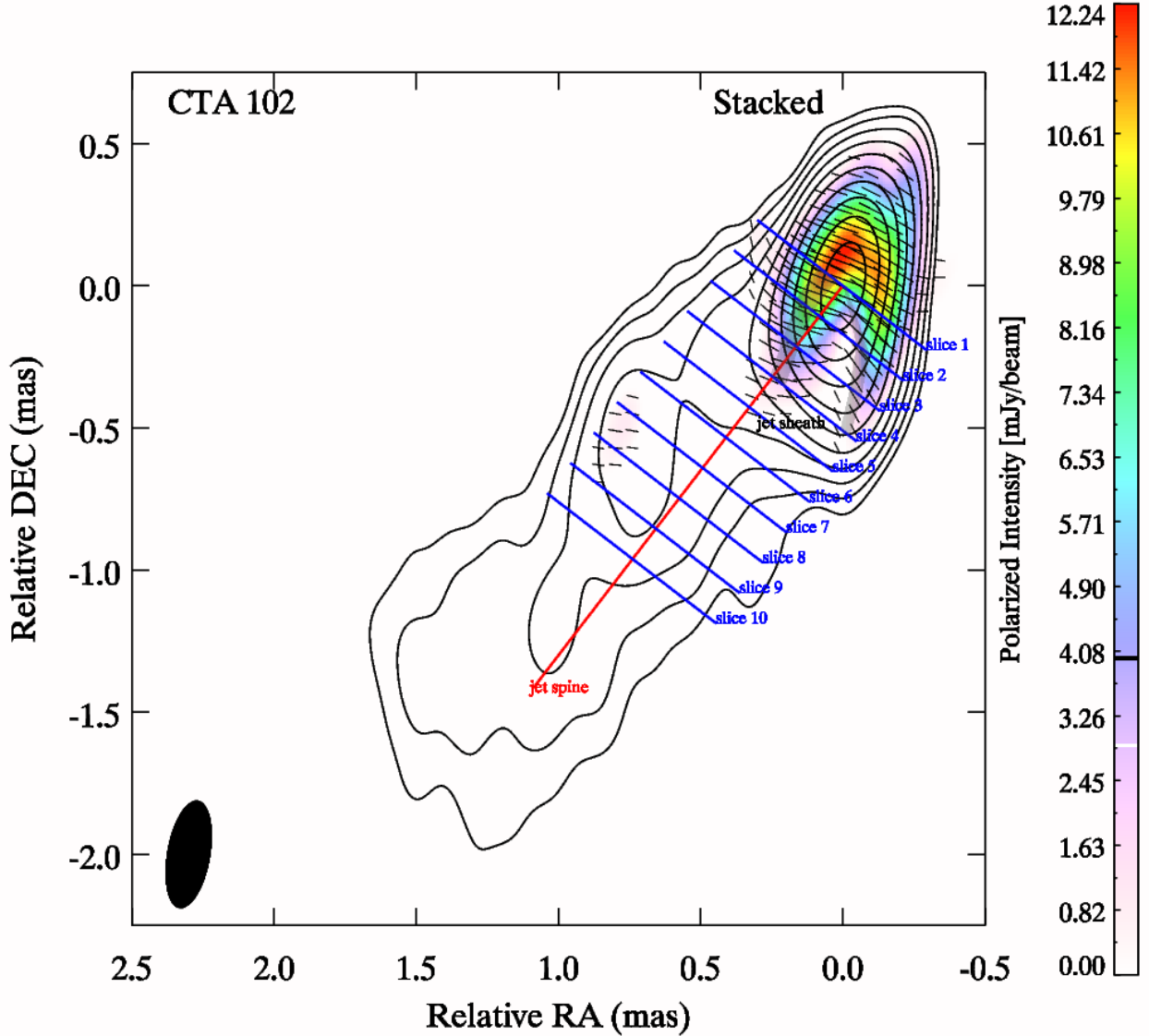


FIG. 16.— A stacked map of 43 GHz images of CTA 102 spanning twenty epochs of observation from 2008 to 2016. The black contours correspond to total intensity (contour levels are: 2.0, 4.0, 8.0, 16.1, 32.2, 64.5, 129.0, 258.1, 516.3, 1032.6 mJy beam⁻¹), whereas the underlying color scheme corresponds to polarized intensity (see color bar to the right for the flux levels), with the EVPAs denoted by black line segments. The EVPAs indicate the orientation of linear polarization as projected onto the plane of the sky. All images have been convolved with a Gaussian beam, shown in the bottom left corner of the stacked map. A jet spine is plotted in red based on the transverse symmetry of the jet, across which ten transverse slices through the data are taken (shown in blue). The profiles of the emission parameters along the second slice are shown in Figure 18. The shaded gray regions in the above map highlight the nominal location of the jet sheath of CTA 102 as determined by the procedure illustrated in Figure 19.

4.5. CTA 102

In Figure 16 we present a stacked radio map of the blazar CTA 102. Similar to 4C 71.07, a continuous polarimetric signature of a jet sheath is evident down the edges of the jet in this stacked radio image. Given the continuous nature of the jet sheath present, we again compute an estimate of the bolometric luminosity of the sheath. The extent of the polarized intensity profile along each of the slices was used to trace the shaded gray regions shown above. This was done by using the width

of the sheath on each side of each slice (shown explicitly in Figure 19) after determining, arbitrarily, the location where the polarized flux falls below 0.85 times the peak value. An estimate of the bolometric luminosity (L_{bol}) of the sheath is computed by adding all of the flux contained within the gray shaded regions of the stacked map above. As in §4.2, we convert this inferred sheath flux at 43 GHz into a spectral luminosity and assume a power-law ($L_{\nu} \propto \nu^{-\alpha}$), which we then integrate from $\nu_{\text{min}} = 10^9$ Hz to $\nu_{\text{max}} = 5 \times 10^{13}$ Hz.

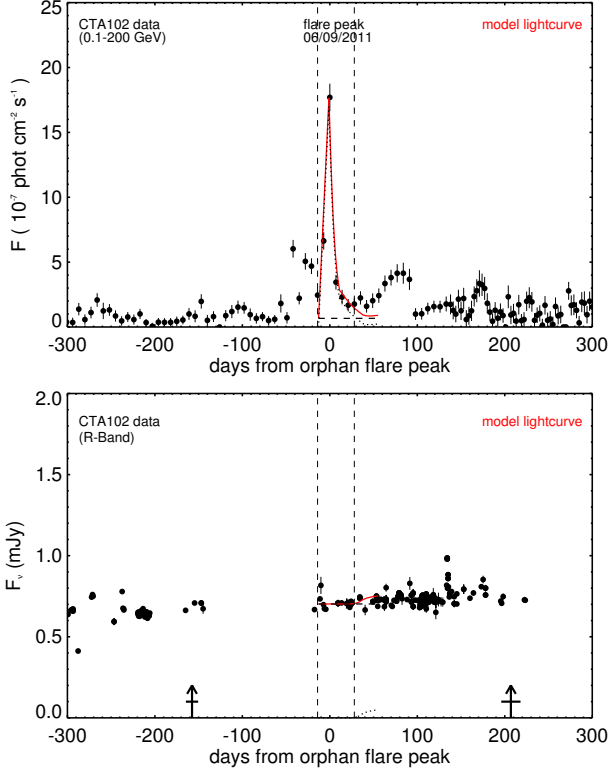


FIG. 17.— Light curves of CTA 102 (black circles) in the γ -rays (upper panel) and optical (lower panel). The model light curves are overlaid in red and consist of the superposition of the model baseline level of flux in each band (the horizontal dashed black line) and the variable emission produced by the model (the dotted black line). The vertical arrows in the lower panel mark the time when superluminal knots passed through the 43 GHz core of CTA 102, with the horizontal bars representing the uncertainty in these times.

Using Equation 1, we obtain: $L_{\text{bol}} \sim 3 \times 10^{45} \text{ erg s}^{-1}$, where we have again assumed a spectral index of $\alpha \sim 1.0$. Similar to 4C 71.07, our estimate above indicates that the jet sheath in CTA 102 is an important source of seed photons even at parsec scales. An estimate of the inner (r_{min}) and outer (r_{max}) radii of the sheath was also obtained: we find that $r_{\text{min}} \sim 0.84 \text{ pc}$ and $r_{\text{max}} \sim 1.28 \text{ pc}$. Similar to the sheath in 4C 71.07, these values are much larger than the inner and outer radii used in our model of the ring (see Table 1) that we posit to exist upstream of the radio core.

The Fermi LAT detected an orphan γ -ray flare from CTA 102 during June 2011 (Figure 17). Table 2 lists the *Ring of Fire* model parameters used to obtain a fit to this orphan flare. The VLBA also observed the ejection of two blobs from the radio core of CTA 102, one occurring roughly 200 days before the onset of the orphan flare and the other roughly 200 days after. The times of the blob ejections are demarcated by vertical arrows in the lower panel of Figure 17. Casadio et al. (2015) performed a detailed analysis of the kinematics of the blobs detected by the VLBA during these epochs and reported bulk Lorentz factors of the order $\Gamma \sim 26$. These VLBI speeds are not all that dissimilar from the blob speed used in our model of this orphan flare ($\Gamma_{\text{final}} \sim 35$). The blob that passed through the core of CTA 102 roughly 200 days after this orphan flare may have supplied the electrons required to scatter the sheath photons.

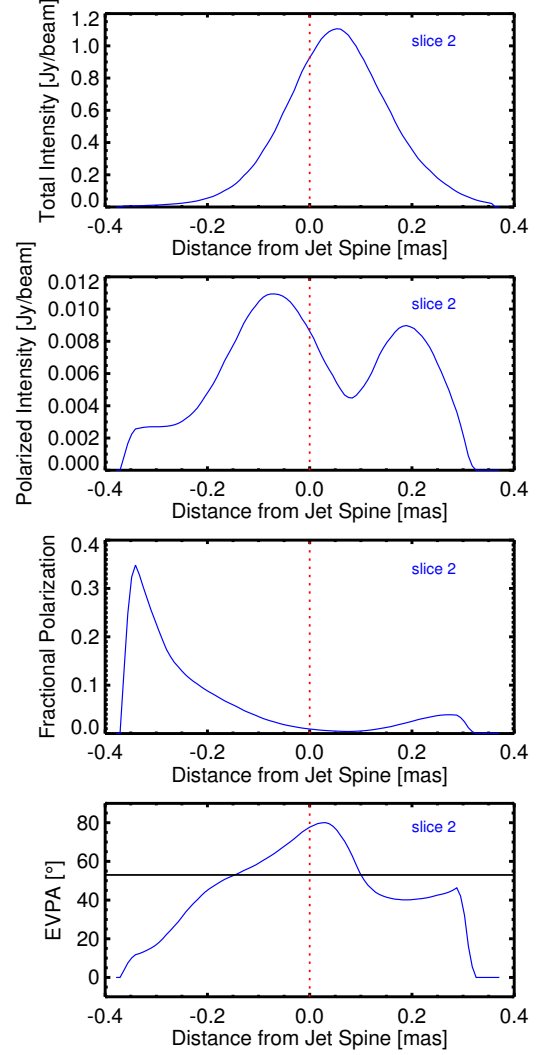


FIG. 18.— Variations of the emission parameters of CTA 102 transverse to the jet axis (dashed red line) for slice 2 (shown in Figure 16) from top to bottom: total intensity, polarized intensity, fractional polarization, and EVPA. The fractional polarization increasing toward the edges of the jet is a predicted polarimetric signature of a jet sheath (as discussed in §1), with the EVPA transverse to the axis. The black line in the lower panel delineates EVPAs that are exactly \perp to the jet spine.

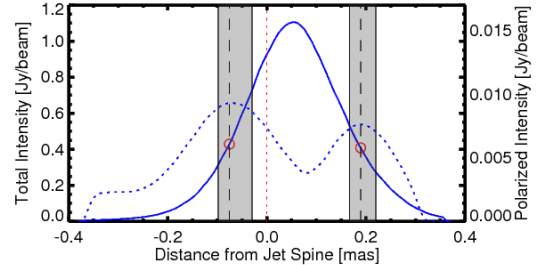


FIG. 19.— The polarized intensity profile of CTA 102 along slice 2 (dashed blue line corresponding to the right-hand axis) is overlaid upon the total intensity profile for slice 2 (solid blue line corresponding to the left-hand axis). We use this double-peaked profile to highlight the likely location of the sheath within each slice (shaded gray regions). The sheath's contribution to the jet's total intensity profile is estimated by the values of total intensity (red circles) that are cospatial with the peaks of the polarized intensity profile (demarcated by dashed vertical lines). This procedure is then repeated for each slice, thus tracing out the sheath (shaded gray regions) shown in Figure 16.

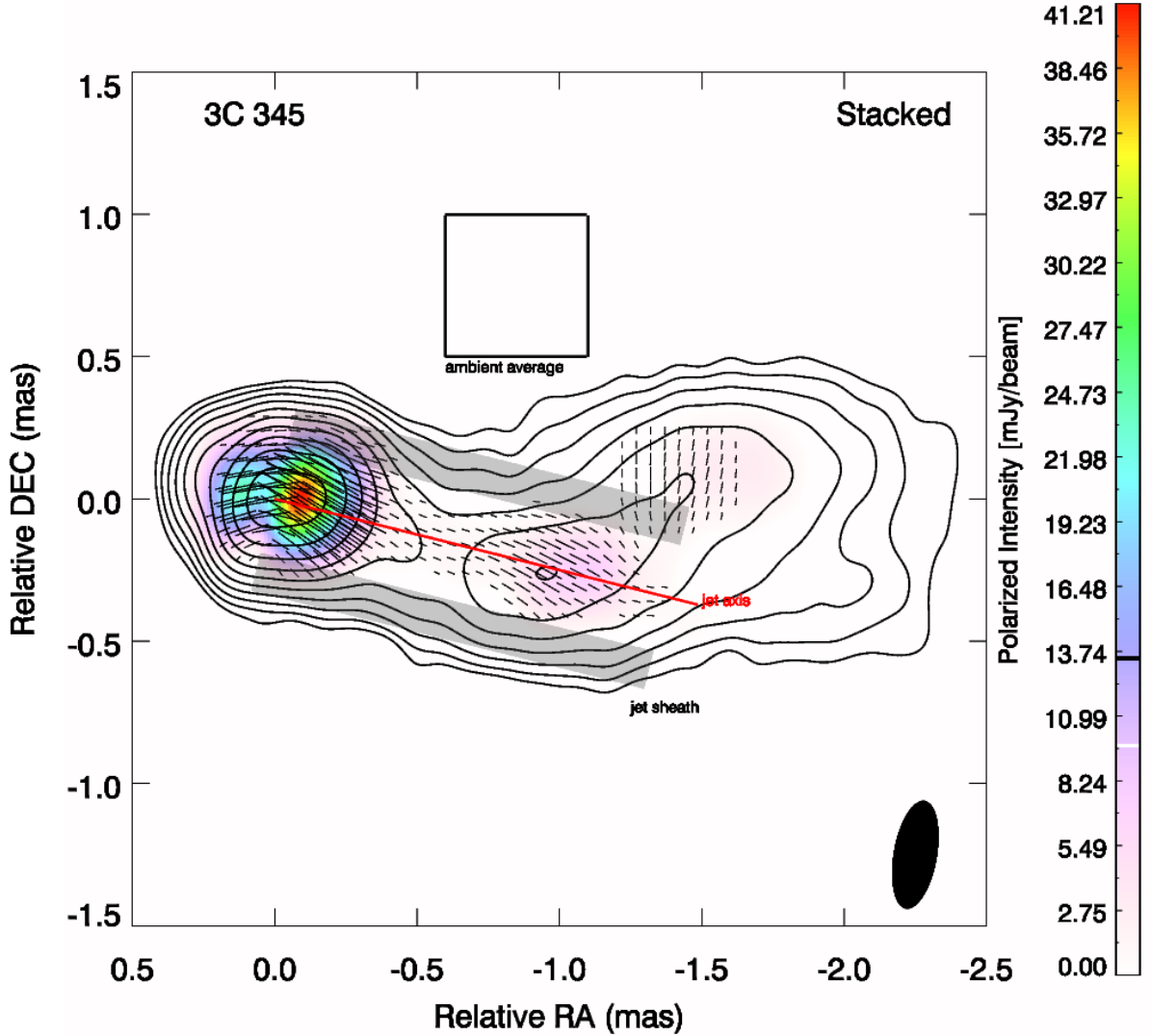


FIG. 20.— A stacked map of 43 GHz images of 3C 345 spanning twenty epochs of observation from 2008 to 2016. The black contours correspond to total intensity (contour levels are: 1.2, 2.4, 4.9, 9.9, 19.9, 39.9, 79.9, 159.8, 319.6, 639.2 mJy beam⁻¹), whereas the underlying color scheme corresponds to polarized intensity (see color bar to the right for the flux levels), with the EVPAs denoted by black line segments. The EVPAs indicate the orientation of linear polarization as projected onto the plane of the sky. All images have been convolved with a Gaussian beam, shown in the bottom right corner of the stacked map. The shaded gray regions in the above map highlight the absence of the polarimetric signature of a jet sheath within 3C 345. The box delineates a region within which we compute an estimate of the ambient noise in this stacked radio map.

4.6. 3C 345

We display a stacked radio map of the blazar 3C 345 in Figure 20. In contrast to the blazars discussed above, there is no polarimetric signature of a jet sheath present in our stacked map. Instead, the polarization is concentrated along the center of the jet, with the EVPAs aligned predominantly parallel to the jet axis. This alignment, in contrast to jet shear, is that expected from diffusive shock acceleration within the jet that compresses the magnetic field and aligns the field lines perpendicular to the jet flow, resulting in EVPAs oriented parallel to the spine of the jet (Wardle et al. 1994). The jet undergoes two bends downstream of the radio core, and the EVPAs

maintain their orientation with respect to the jet axis around each bend. We searched through archival γ -ray and optical light curves to look for instances of orphan γ -ray flares within 3C 345. We were unable to find any (see Figure 21). This suggests that an enhancement in the jet sheath is not present within 3C 345. The lack of a polarimetric signature of a jet sheath within 3C 345 might indicate that, while jet sheaths are almost certainly present within all blazars, the sheath itself only becomes “enhanced” at certain times within the span of a blazar’s lifetime (perhaps as a portion of the sheath encounters a standing shock within the jet). This would explain why the majority of blazar γ -ray flares are not orphan in na-

ture. It is also possible that the jet sheath is present, but we are unable to detect it due to the extreme gradient in intrinsic brightness between the spine and the sheath. In order to compute a rough estimate of the upper limit of the bolometric luminosity of a jet sheath within 3C 345, we trace (in gray) a region on the periphery of the jet within which a sheath might exist (see Figure 20). Similar to §4.2, we add up the flux in these gray sheath regions at 43 GHz, but instead of using jet flux we use an estimate of the ambient noise in our stacked map (obtained within the box shown in Figure 20). Using Equation 1, we obtain an upper limit to the bolometric luminosity of a sheath of $L_{\text{bol}} \sim 5 \times 10^{42} \text{ erg s}^{-1}$, where we have again assumed a spectral index of $\alpha \sim 1.0$ and limits of integration of $\nu_{\text{min}} = 10^9 \text{ Hz}$ and $\nu_{\text{max}} = 5 \times 10^{13} \text{ Hz}$. The majority of the stacked maps presented in this paper are comprised of twenty epochs of observation. It might be profitable to continue stacking to see whether additional maps yield a still fainter signature of a jet sheath within 3C 345.

5. SUMMARY AND CONCLUSIONS

We have created stacked 43 GHz maps of the milliarcsecond-scale structure of the total and polarized intensity of the blazars 3C 273, 4C 71.07, 3C 279, 1055+018, CTA 102, and 3C 345. Each stacked map is carefully constructed from data collected over the course of eight years as part of the VLBA-BU-BLAZAR program, creating images with unprecedented dynamic range, sensitivity, and angular resolution. We find the polarimetric signature of a jet sheath within five of these stacked radio maps. In the stacked radio map within which we did not detect the polarimetric signature of a jet sheath (3C 345 - Figure 20), we were also unable to find any instances of orphan γ -ray flares. This perhaps indicates that localized enhancements within the jet sheath, required by the *Ring of Fire* model, persist only for a short period of time. This would explain why the majority of γ -ray flares detected within blazars are not orphan in nature. The five blazars (3C 273, 4C 71.07, 3C 279, 1055+018, and CTA 102) in which we detect a jet sheath have all exhibited orphan flaring behavior.

The *Ring of Fire* model, developed by MacDonald et al. (2015), is able to reproduce the basic time profiles of these orphan flares. This model invokes the presence of a localized enhancement within the jet sheath (a shocked segment/ring) to create a source of seed photons that are inverse-Compton scattered up to high energies by electrons contained within a blob moving relativistically along the jet spine and through the enhancement. By simply varying the nature of the blob's acceleration down the spine of the jet, we are able to obtain fits to all five of these orphan flare profiles. This highlights the potential of the *Ring of Fire* model to explain all orphan γ -ray flaring behavior from within blazars based on the radiative interplay between plasma sheaths and plasma blobs within these relativistic jets. As discussed in MacDonald et al. (2015), we find no conflict (as suggested by Nalewajko et al. 2014) in the sheath's ability to supply sufficient levels of seed photons for inverse-Compton scattering while not simultaneously outshining the jet spine. The six orphan flares we present in this paper were contemporaneous with radio blob ejections detected by analysis of VLBA images (Figures 4, 7, 11,

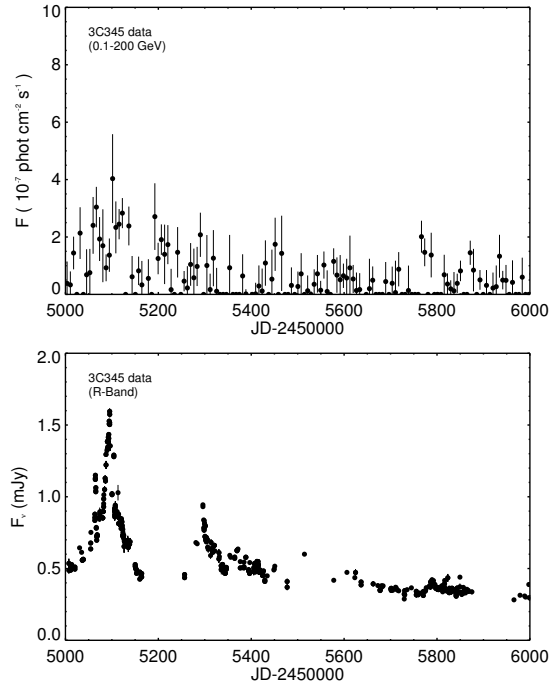


FIG. 21.— Light curves of 3C 345 (black circles) in the γ -rays (upper panel) and optical (lower panel). In contrast to the orphan flare profiles presented in sections §4.1–§4.5, here there is little evidence of prominent orphan γ -ray flaring activity.

14, & 17), thus lending further observational support to the plausibility of our model. A rough estimate of the location(s) in the jet of the enhancement in the photon field of the sheath (i.e., the ring) can be obtained from the time (Δt) between the respective orphan flare peaks and when each blob passed through the radio core. If we assume, for simplicity, that the blob travels with a constant velocity (β_{app}) along the jet, then the distance Δz upstream/downstream of the flare from the radio core is given by

$$\Delta z \simeq \frac{\beta_{\text{app}} \Delta t c}{\sin(\theta_{\text{obs}})}. \quad (2)$$

The values obtained from Equation 2 for the orphan flares presented in §§4.1–4.5 are listed in Table 2. Our model allows for a different location of γ -ray flare production within the jet than those considered in most interpretations of blazar light curves, namely, the BLR, a dusty torus, or a standing shock in the millimeter-wave “core” (e.g., Marscher 2014; Joshi, Marscher & Böttcher 2014).

ACKNOWLEDGEMENTS

Funding for this research was provided by a Canadian NSERC PGS D2 Doctoral Fellowship and by NASA Fermi Guest Investigator grants NNX11AQ03G, NNX12AO79G, NNX12AO59G and NNX14AQ58G. The authors are grateful to Karen Williamson for compiling the multi-wavelength data used in Figures 4, 7, 11, 14, 17, and 21. The VLBA is an instrument of the National Radio Astronomy Observatory. The National Radio Astronomy Observatory is a facility of the National Science Foundation operated under cooperative agreement by Associated Universities, Inc.

TABLE 2
RING OF FIRE SOURCE PARAMETERS

	3C 273	4C 71.07	3C 279	1055+018	CTA 102
Γ_{initial}	3.0	3.0	2.0	4.0	2.0
Γ_{final}	25.0	10.0	20.0	20.0	35.0
z_{initial} (pc)	-0.4	-0.4	-0.1	-0.6	-0.2
z_{final} (pc)	0.0	0.0	0.1	0.16	0.0
$P_{\text{inj flare1}}$ (ergs s $^{-1}$)	5.0×10^{45}	1.0×10^{45}	3.0×10^{44}	3.0×10^{44}	4.6×10^{45}
$P_{\text{inj flare2}}$ (ergs s $^{-1}$)	-	9.0×10^{44}	-	-	-
Baseline Flux _{optical} (mJy)	28.7	0.7	3.8	0.64	0.7
Baseline Flux _{γ-ray} (10^{-7} phot cm $^{-2}$ s $^{-1}$)	1.7	0.76	6.5	0.67	0.67
Z	0.158	2.17	0.538	0.89	1.037
θ_{obs}	6.1 $^{\circ}$	3.0 $^{\circ}$	2.1 $^{\circ}$	2.0 $^{\circ}$	2.6 $^{\circ}$
Δz (pc)	0.4	29.8	27.4	77.0	96.2
relative to radio core	downstream	upstream	downstream	upstream	upstream

REFERENCES

- Aharonian, F., Akhperjanian, A. G., Bazer-Bachi, A. R., et al. 2007, *ApJL*, **664**, L71
- Casadio, C., Gómez, J. L., Jorstad, S. G., et al. 2015, *ApJ*, **813**, 51
- Cawthorne, T. V., & Cobb, W. K. 1990, *ApJ*, **350**, 536
- Cawthorne, T. V., Jorstad, S. G., & Marscher, A. P. 2013, *ApJ*, **772**, 14
- Dodson, R., Rioja, M. J., Molina, S., & Gómez, J. L., 2016, *ApJ*, submitted
- Fromm, C. M., Ros, E., Perucho, M., et al. 2013, *A&A*, **557**, A105
- Gabuzda, D. C., Reichstein, A. R., & O'Neill, E. L. 2013, *MNRAS*, **444**, 172
- Georganopoulos, M., & Kazanas, D. 2003, *ApJL*, **594**, L27
- Homan, D. C., Lister, M. L., Kovalev, Y. Y., et al. 2015, *ApJ*, **798**, 134
- Jorstad, S. G., Marscher, A. P., Lister, M. L., et al. 2005, *AJ*, **130**, 1418
- Jorstad, S. G., Marscher, A. P., Smith, P. S., et al. 2013, *ApJ*, **773**, 147
- Joshi, M., & Böttcher, M. 2011, *ApJ*, **727**, 21
- Joshi, M., Marscher, A. P., & Böttcher, M. 2014, *ApJ*, **785**, 132
- Kardashev, N. S. 1962, *SvA*, **6**, 317
- Lavaux, G., & Hudson, M. J. 2011, *MNRAS*, **416**, 2840
- Lyutikov, M., Pariev, V. I., & Gabuzda, D. C. 2005, *MNRAS*, **360**, 869
- MacDonald, N. R., Marscher, A. P., Jorstad, S. J., et al. 2015, *ApJ*, **804**, 111
- Marscher, A. P., Jorstad, S. G., D’Arcangelo, F. D., et al. 2008, *Nature*, **452**, 966
- Marscher, A. P., Jorstad, S. G., Larionov, V. M., et al. 2010, *ApJ*, **710**, L126
- Marscher, A. P., Jorstad, S. G., Agudo, I., MacDonald, N. R., & Scott, T. L. 2012, in *eConf C1111101*, *Fermi & Jansky: Our Evolving Understanding of AGN*, ed. R. Ojha, D. Thompson, & C. D. Dermer ([arXiv:1204.6707](https://arxiv.org/abs/1204.6707))
- Marscher, A. P. 2014, *ApJ*, **780**, 87
- Nalewajko, K., Begelman, M. C., Sikora, M. 2014, *ApJ*, **789**, 161
- Wardle, J. F. C., Cawthorne, T. V., Roberts, D. H., & Brown, L. F. 1994, *ApJ*, **437**, 122
- Williamson, K. E., Jorstad, S. G., Marscher, A. P., et al. 2014, *ApJ*, **789**, 135
- Zamaninasab, M., Savolainen, T., Clausen-Brown, E., et al. 2013, *MNRAS*, **436**, 3341